Journal of Power Sources 212 (2012) 57–65

Contents lists available at SciVerse ScienceDirect

Journal of Power Sources

journal homepage: www.elsevier.com/locate/jpowsour

Electrodeposited osmium three-dimensional anodes for direct borohydride fuel cells

V.W.S. Lam [a,c], D.C.W. Kannangara [a], A. Alfantazi [b], E.L. Gyenge [a,c,*]

[a] Department of Chemical and Biological Engineering, The University of British Columbia, 2216 Main Mall, Vancouver, B.C. V6T 1Z3, Canada
[b] Department of Materials Engineering, The University of British Columbia, Vancouver, B.C. V6T 2E8, Canada
[c] Clean Energy Research Centre, The University of British Columbia, Vancouver, B.C. V6T 1Z3, Canada

ARTICLE INFO

Article history:
Received 25 January 2012
Received in revised form
22 March 2012
Accepted 23 March 2012
Available online 10 April 2012

Keywords:
Direct borohydride fuel cell
Electrodeposition
Three-dimensional electrode

ABSTRACT

Three-dimensional Os anodes for direct borohydride fuel cells (DBFC) were developed by surfactant assisted electrodeposition of Os on two fibrous graphite substrates, AvCarb™ P75 and GF-S3, respectively. Structural characterization of the electrodes using SEM, TEM, and XPS revealed cluster-like Os deposits composed of nano-sized particles of less than 5 nm in diameter with partially oxidized surfaces. The structural and compositional features of the graphite fiber matrixes had a profound influence on the crystallography of the electrodeposited Os. The polycrystalline Os/AvCarb™ P75 exhibited superior electrocatalytic activity in cyclic voltammetry compared to Os/GF-S3 with respect to oxidation of adsorbed intermediates. To explain the different activity XRD was used to investigate the crystallographic differences between the two electrodes. A DBFC with Nafion® 117 membrane and operated at 333 K, with Os/AvCarb™ P75 anode (1.7 mg cm^{-2} Os) and 4 mg cm^{-2} Pt black oxygen cathode catalyst, generated a peak power density of 109 mW cm^{-2} with a standard error of the mean of ±12 mW cm^{-2} at 90% confidence level. The longer-term durability of the newly developed anodes was investigated.

1. Introduction

Direct fuel cells have found emerging applications in portable electronics, where there is a growing demand for high energy density power supplies. Organic fuels such as methanol and ethanol suffer generally from slow electrooxidation kinetics and catalyst deactivation via CO_{ad} poisoning, requiring typically high precious metal catalyst loadings [1,2]. Alternative to organic fuels are inorganic alkaline solutions of hydrazine [3] and borohydrides [4]. These are attractive fuels due to high theoretical energy density (9.3 W h g^{-1} and 5.4 W h g^{-1} for borohydride and hydrazine respectively) and the lack of carbonaceous species. The absence of carbon in the fuel eliminates the catalyst poisoning by CO formation and adsorption. As a result, the durability of the fuel cell anode could be extended.

Similar to other fuel cell systems, many DBFC studies employed expensive noble metal catalysts such as Pt [4]. The price of Pt has been climbing since 1999 and it is currently (December 2011) at ~$49 USD per gram [5]. The inability for fuel cell systems to move away from Pt or Pt based catalysts is a hindrance in their commercialization. In order to reduce the Pt loadings, previously we have investigated the applicability of graphite felt supported three-dimensional PtRu anodes (3:2 atomic ratio) for the DBFC system [6]. In comparison to Vulcan® XC72 carbon supported and non-supported PtRu catalysts layers coated on Nafion® 117, it was found that both the electrode kinetic and mass transport performance was significantly improved when using the PtRu/graphite felt anode with a thickness of 350 μm. At 333 K a peak power density of 130 mW cm^{-2} was achieved for the PtRu/graphite felt compared to 80 mW cm^{-2} and 35 mW cm^{-2} for PtRu/ Vulcan® XC72 and PtRu black, respectively, at 1 mg cm^{-2} total catalyst loadings [6]. We proposed that the presence of Nafion® in the DBFC anode catalyst layer was redundant in the presence of the 2 M NaOH electrolyte and moreover, the Nafion® may in fact impede the mass transport of borohydride anions to catalytic sites. Furthermore, in the thicker three-dimensional electrode the residence time of the anolyte (0.5 M $NaBH_4$–2 M NaOH) increased, potentially resulting in higher utilization efficiency of BH_4^-.

Three-dimensional electrodes have been extensively developed for direct organic fuel cells [7–19]. Bauer et al. produced active PtRu three-dimensional electrodes for methanol electrooxidation on graphite felts; such as GF-S3, by a non-ionic surfactant (Triton-X 100) mediated electrodeposition [10,12]. These authors also

* Corresponding author. Department of Chemical and Biological Engineering, The University of British Columbia, 2216 Main Mall, Vancouver, B.C. V6T 1Z3, Canada. Tel.: +1 604 822 3217; fax: +1 604 822 6003.
E-mail address: egyenge@chbe.ubc.ca (E.L. Gyenge).

0378-7753/$ – see front matter © 2012 Elsevier B.V. All rights reserved.
doi:10.1016/j.jpowsour.2012.03.067

discussed the differences between flow-by and flow-through configurations for three-dimensional direct methanol fuel cell anodes [14].

The objective of the present study is to explore the three-dimensional anode concept for DBFC for the case of Os nanoparticle catalysts. The effectiveness for BH_4^- oxidation of Vulcan® XC72 supported Os nanoparticles synthesized by the Bönneman was demonstrated by Atwan et al. [20,21] and Lam and Gyenge [22]. The latter authors determined by voltammetry a seven-electron BH_4^- oxidation on Os/C accompanied by reduced hydrogen evolution compared to Pt/C and PtRu/C. DBFC experiments using Os/C catalyst layer coated on Nafion® 117 membrane, revealed that at 298 K the BH_4^- electrooxidation on 20 wt% Os/C was superior to commercial 20 wt% Pt/ C and PtRu/C in the electrode kinetic controlled and mass transport regions of the polarization curves [22]. A recent theoretical study of BH_4^- on Os (111) surface revealed strong undissociative adsorption [23], which could be favorable for direct electrooxidation of BH_4^- as opposed to its hydrolysis followed potentially by oxidation of the evolved H_2.

2. Experimental methods

AvCarb™ P75 (uncompressed thickness of about 210 μm and porosity of 0.85, supplied by FuelCellStore.com) and GF-S3 (uncompressed thickness of 350 μm and porosity of 0.95, supplied by Electro-Synthesis Company Inc.) were used as deposition substrates. Prior to electrodeposition of the Os catalyst, the substrates were electrochemically pretreated in 2 M NaOH by potential cycling between 0 and 2 V_{SHE} for 50 cycles at 50 mV s^{-1} at 295 K using Ti counter electrodes and Hg/HgO/0.1 M KOH reference electrode. The substrates were then thoroughly rinsed with 18 MΩ deionized water and air-dried at 333 K in an oven. The Os electrodeposition media consisted of a 10 mM $(NH_4)_2OsCl_6$ (Alfa Aesar) solution prepared with 18 MΩ deionized water. Triton-X 102 (12.5 vol%) (Sigma Aldrich) was added to control the deposit morphology and structure. The electrodeposition media composed of Triton-X 102 and $(NH_4)_2OsCl_6$ solution was heated and stirred on a hot plate at 341 K for at least 30 min prior to deposition. Any evaporation of solution during the pre-heating procedure was replaced with 18 MΩ deionized water.

Electrodeposition was carried out at 341 K at a constant specified current density of 4 mA cm^{-2} for 30 min. At the end of the Os deposition, the substrate was removed and soaked in acetone for 10 min at 330 K. After soaking in acetone, the substrate was refluxed in 50:50 v/v hexane and acetone for 1 h at 363 K to remove the surfactant Triton-X 102 from the surface of the three-dimensional electrode. Afterwards, the substrate was dried in air at 295 K.

When more than one electrodeposition step was performed on the same substrate, the substrate was washed in acetone at 330 K for 10 min between depositions. Reflux cleaning was only applied at the very end of the complete electrodeposition procedure.

The morphology and structure of the Os electrodeposit were characterized by XPS (Leybold Max 200 andKratos AXIS Ultra), TEM (FEI Tecnai G2 200 kV Transmission Electron Microscope), XRD (D8 Advance Brukerdiffractometer with Cu $K\alpha_1$ source), SEM (Hitachi S-4700 and Hitachi S-4500 Field Emission Scanning Electron Microscopes), and ICP-MS for Os loading determination.

For half-cell electrochemical evaluation of the electrocatalytic activity toward BH_4^- oxidation of the Os electrodeposited GF-S3 and AvCarb P75, solutions of 10 mM $NaBH_4$ were prepared using a powdered form of 98%+ $NaBH_4$ (Acros Inc.) in 2 M NaOH. A three-electrode setup composed of the Os three-dimensional working electrode (6.5 cm^2 geometric area) with Ag/AgCl/3 M KCl reference electrode (Cypress Systems Inc.) and a platinized titanium counter electrode (6.45 cm^2 geometric area) was connected to a PARSTAT 2263 potentiostat (Princeton Applied Research). For the voltammetry data, in each electrolyte composition (i.e., 2 M NaOH or 10 mM $NaBH_4$–2 M NaOH), 50 scans were run at 50 mV s^{-1} prior to 10 slow scans at 10 mV s^{-1}. The 60th scan in each test is presented here.

Fuel cell experiments were conducted using the Fideris MTK test station. The membrane electrode assembly comprised of the Os electrodeposited AvCarb P75 or GF-S3 anode and a Nafion® 117 membrane with 4 mg cm^{-2} Pt black on the cathode side (Lynntech Inc.). The end plate material was stainless steel with a serpentine flow field. Flow rates for the anolyte (0.5 M $NaBH_4$–2 M NaOH) and oxidant (O_2) were 10 mL min^{-1} and 0.25–1.25 SLPM (i.e., l min^{-1} at 273 K, 1 atm), respectively. The O_2 absolute pressure was 4.4 atm, while the anode side pressure was about 1 atm. Temperatures used during fuel cell performance testing were 298 K or 333 K.

3. Results and discussion

3.1. Pretreatment of the fibrous carbon substrates by potential cycling in 2 M NaOH

The AvCarb™ P75 and GF-S3 substrates before and after pretreatment were analyzed using XPS. The pretreatment procedure is described in Section 2. Elemental analysis of the untreated AvCarb™ P75 substrate shows much lower content of heteroatoms (particularly oxygen and nitrogen) as compared to untreated GF-S3, which contains approximately 72 wt% carbon and 23 wt% oxygen (Table 1). After pretreatment, the surface oxygen content of AvCarb™ P75 increased by about 6 wt%, indicating oxidation of the substrate forming functional groups such as C–OH, C=O, COO–, which were also separately identified by deconvolution of the carbon spectra. The pretreatment of the GF-S3 substrate on the other hand resulted in a decrease of the oxygen content with about 4 wt% (Table 1), which suggest possible electro-oxidation of functional groups on graphite felt (such as C–OH and COOH) to $CO_{2,(g)}$. After pretreatment, the oxygen content of GF-S3 is approximately three times that of AvCarb™ P75 and the former also contains nitrogen in higher proportion (Table 1). The surface oxygen and nitrogen functional groups could act as active sites for Os nucleation and deposition.

3.2. Os electrodeposition and structural characterization

Fig. 1 shows the cathode potential profile during the electrodeposition of Os on the AvCarb™ P75 substrate. There appears to be two deposition stages. The first stage, shown in the first 20–30 s in the inset of Fig. 1, involves the nucleation of Os deposits on

Table 1
Elemental composition (in wt%) of the three-dimensional fibrous carbon deposition substrates before and after pretreatment.

Sample	C	Ca	Cl	N	Na	O	S	Si
AvCarb™ P75	98.4–99.4	–	–		–	0.6–1.6	–	–
Pretreated AvCarb™ P75	90.7–91.4	–	0.1	0.2–0.5	1.6–2.3	6–7.3	–	–
GF-S3	70.7–72.2	0.5–0.8		3.1–3.2	1.0–1.2	21.7–23.4	0.6	0.2–0.6
Pretreated GF-S3	75.1–76.1	0.4–0.5		4–4.4	0.7–1.1	18.3–18.5	0.1	0.3–0.4

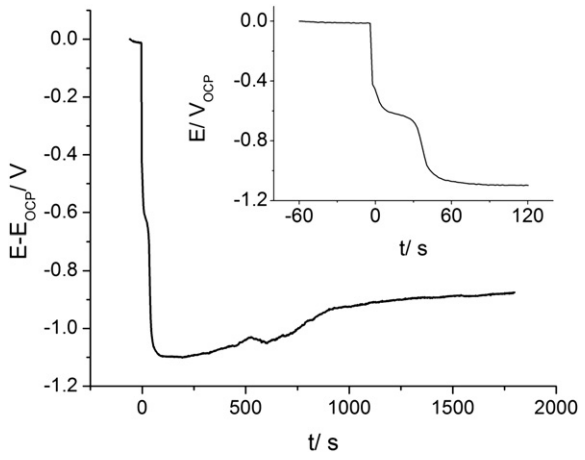

Fig. 1. Cathode potential profile during Os electrodeposition on AvCarb™ P75 substrate at 4 mA cm^{-2} and 341 K. Inset shows the cathode potential profile during the first 120 s of deposition. The bath was composed of 10 mM $(NH_4)_2OsCl_6$ with 12.5 vol% of Triton-X 102 OCP = open-circuit potential.

energetically favorable sites. From ∼30 s onward, the second stage involves the bulk deposition of Os. At deposition times much greater than 30 min (not shown here), severe mass transport limitation is imposed by the depletion of Os salt concentration within the deposition substrate. It should be noted that the electrodeposition media was not stirred. A similar profile to Fig. 1 was observed when electrodepositing Os onto the GF-S3 substrate.

SEM images of AvCarb™ P75 and GF-S3 are shown in Fig. 2A and B, respectively. Fig. 2C and D shows the respective substrates with electrodeposited Os. The unique structural feature of the AvCarb P75 is the presence of interstitial carbon deposit in the form of rough plates among the fibers (compare Fig. 2A and B). These interstitial carbon plates appear to be favorable sites for electrodeposition on AvCarb P75 as shown by Fig. 2C. For GF-S3, dense and fairly uniform deposition of aggregates occurred on the fiber (Fig. 2D). Low magnification SEM images (not shown here) revealed a fairly homogeneous distribution of the Os deposits throughout the thickness of both substrates.

Upon closer inspection of the electrodes with TEM (Fig. 3A and B), it was found that the larger deposits are actually agglomerates composed of nano-sized Os particles, with particle sizes of 5 nm or lower. A similar morphology was observed in our previous study of electrodeposited PtRu on GF-S3 using a similar electrodeposition procedure [6]. The Os nanoparticle distribution within the aggregate appeared to be more uniform in case of GF-S3, which could be explained by the higher proportion of surface heteroatoms (particularly oxygen and nitrogen) (Fig. 3B vs. 3A, and Table 1).

Fig. 4 shows the XRD spectra from $2\theta = 34–90$ for an Os/AvCarb™ P75 electrode with a metal loading of 0.3 mg cm^{-2} and an Os/GF-S3 electrode with a metal loading of 0.2 mg cm^{-2}. The spectra for the Os/GF-S3 electrode indicates the presence mainly of the (101) plane with a low intensity compared to the strongly polycrystalline Os/AvCarb™ P75 where the (100), (101), (103), (110) and (111) planes could be identified. Among the latter planes, the (101) plane generated the highest intensity. The crystallite sizes for the Os/AvCarb™ P75 and Os/ GF-S3 electrodes were calculated to be approximately 2 nm. Another interesting distinguishing feature between the two electrodes is the strong graphite XRD signal from AvCarb™ P75 and its absence in case of GF-S3 (Fig. 4). This shows significant structural differences between the two graphitic substrates, with possibly a high content of amorphous-like (less ordered) graphite in case of GF-S3.

3.3. Cyclic voltammetry investigation of borohydride oxidation on the electrodeposited three-dimensional Os electrodes

Fig. 5A and B shows the cyclic voltammogram of Os/AvCarb™ P75, and Os/ GF-S3 respectively, in 2 M NaOH in the absence and presence of borohydride. The broad anodic peaks in the absence of borohydride at −0.56 V in Fig. 5A (dashed line) and −0.59 V in Fig. 5B (dashed line) represent the electrooxidation of H_2 generated

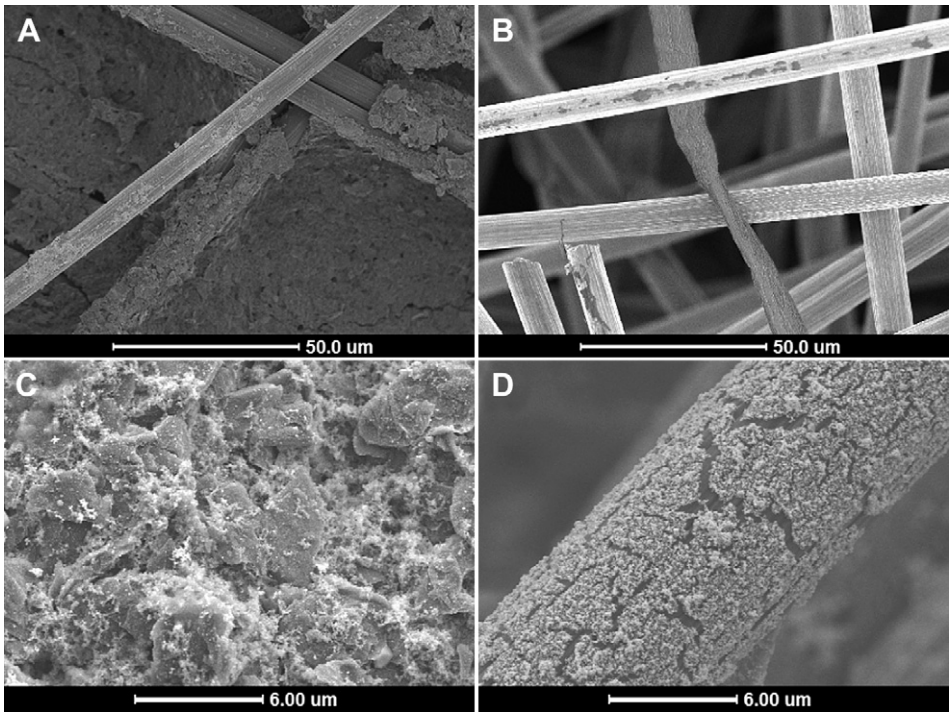

Fig. 2. SEM images of (A) AvCarb™ P75 without deposit, (B) GF-S3 without deposit, and Os electrodeposited on: (C) AvCarb™ P75 and (D) GF-S3 substrates.

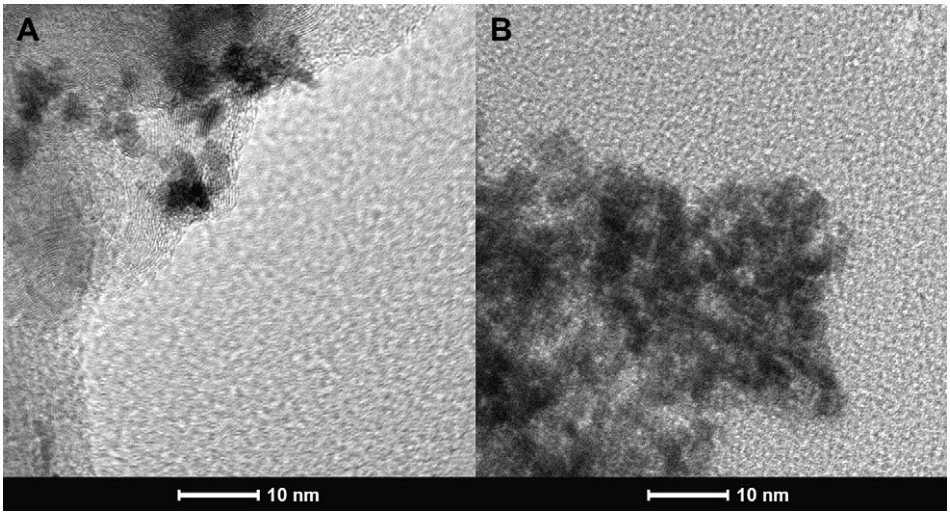

Fig. 3. TEM images of Os deposits on (A) AvCarb™ P75 and (B) GF-S3 substrates.

at the cathodic starting potential of −0.9 V. Fig. 5A (dashed line), also reveals that on Os/AvCarb™ P75 weak underpotential formation of hydrogen occurred on the reverse cathodic scan between approximately −0.57 V and −0.77 V, which was absent for the Os/GF-S3 electrode (Fig. 5B (dashed line)). The strongly polycrystalline Os/AvCarb™ P75 surface (Fig. 4) is more likely to generate underpotentially deposited hydrogen atoms. Furthermore, there were no Os oxidation peaks within the potential range of the cyclic voltammograms, although the formation of OsO_2 is thermodynamically favorable at high pH and at potentials greater than −0.3 V [24].

When 10 mM $NaBH_4$ was added to the 2 M NaOH solution, on the Os/AvCarb™ P75 electrode two characteristic oxidation peaks were observed, one at −0.48 V in the anodic direction and the other at −0.43 V on the return cathodic scan (Fig. 5A (solid line)). For the Os/GF-S3 electrode, there was a slight positive shift for the forward oxidation peak to −0.44 V, whereas the cathodic return scan oxidation peak remained at −0.43 V (Fig. 5B (solid line)). The anodic peak currents (expressed as Os mass specific activities) on both electrodes were between about 3–4 times larger with BH_4^- in 2 M NaOH. This shows clearly the activity of the electrodeposited Os electrodes toward BH_4^- electrooxidation.

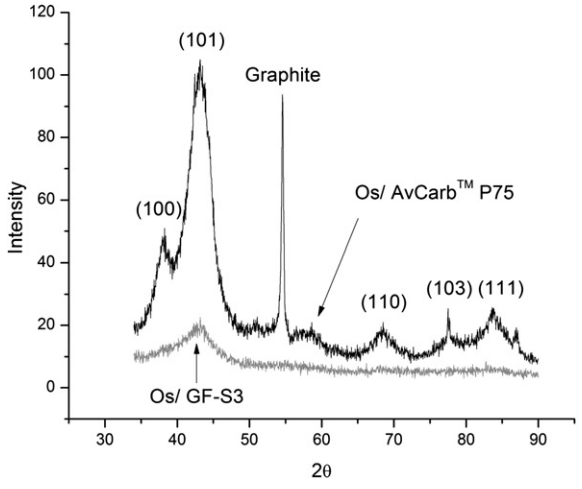

Fig. 4. XRD wide scan of Os electrodeposited onto AvCarb™ P75 (Os loading: 0.3 mg cm^{-2}) and GF-S3 (Os loading 0.2 mg cm^{-2}).

The observed peaks on Os/AvCarb™ P75 in the presence of BH_4^- (Fig. 5A (solid line)) are similar in appearance to the characteristic dominant peaks "*a1*" (on the anodic scan) and "*c1*" (cathodic return scan) found on Pt [25]. Recent literature has suggested that the BH_4^- electrooxidation reactions on Pt occurring at the "*a1*" and "*c1*" peaks are complex from a mechanistic point of view [26–28]. The "*a1*" peak has been attributed to the composite oxidation of $BH_{4\,ad}^-$ and H_{ad}, the latter formed also through partial hydrolysis of BH_4^- [26]. For Os nanoparticles prepared by a modified Bönneman method and supported on Vulcan® XC72, Lam and Gyenge reported a seven electron oxidation of BH_4^- corresponding to peak "*a1*" through analysis of the peak current and potential of their voltammetry data [22]. In the present work, the number of electrons associated with the voltammetric peaks from Fig. 5A and B was not determined because application of the standard voltammetry theory to responses from three-dimensional electrodes was deemed unreliable. A detailed electrode kinetic model for the BH_4^- oxidation on three-dimensional electrodes is very much required in future work corroborated by experiments using electrodeposited Os RDE to establish the total number of electrons involved and to assess the feasible mechanistic pathways.

A notable difference between Os on AvCarb™ P75 and GF-S3 is the shape of oxidation peak "*c1*" on the return cathodic scan (Fig. 5A and B (solid lines)). For Os/GF-S3, this peak is broader and its peak current is over two times smaller than on Os/AvCarb™ P75. The "*c1*" peak has been attributed to oxidation of strongly adsorbed intermediates such as BOH_{ad} and BH_2OH_{ad} [26]. The broader peak on Os/GF-S3 could be indicative of a wider range of adsorbed species present on the surface compared to the Os/AvCarb™ P75, where a sharp "*c1*" peak was observed. Furthermore, the large "*c1*" oxidation peak current density for Os/AvCarb™ P75 suggests more effective oxidation of the adsorbed intermediates. For Os/GF-S3 the BH_4^- cyclic voltammogram was similar to that on Os nanoparticles prepared by a modified Bönneman method and supported on Vulcan® XC72 [22].

To better understand the Os/AvCarb™ P75 surface, XPS was performed after the electrode had been subjected to electrochemical half-cell tests (Fig. 6). A narrow scan was performed on the Os 4f double peak. Deconvolution revealed four peaks with binding energies at 50.8 eV, 51.7 eV, 53.5 eV, and 54.4 eV. It was found that the binding energies at 50.8 eV and 53.5 eV corresponded to the literature values indicating the presence of Os(0) ($4f_{7/2}$ and $4f_{5/2}$, respectively) [29–33]. The binding energies at

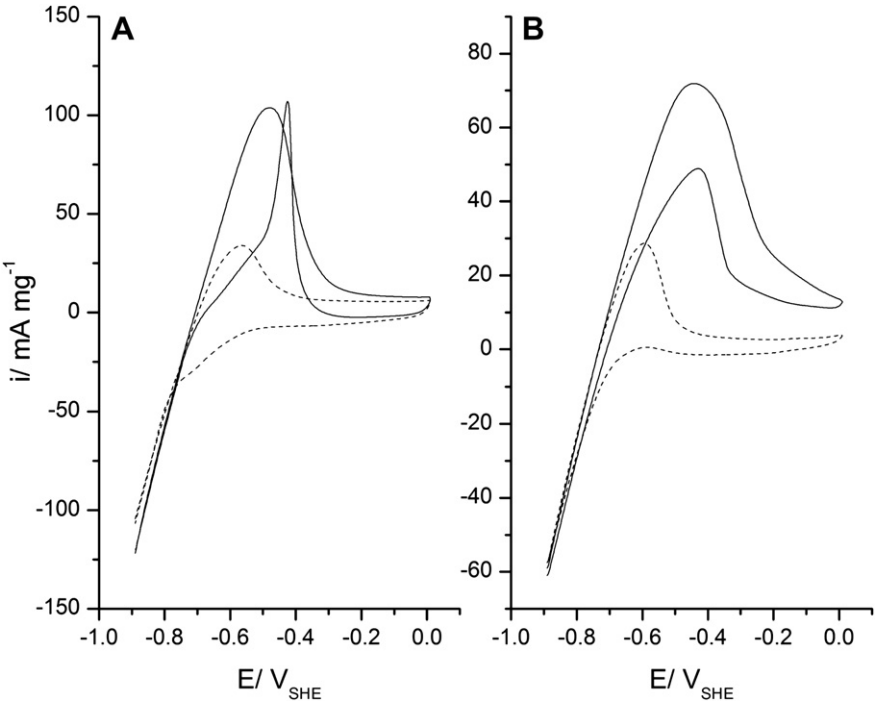

Fig. 5. Cyclic voltammogram of (A) Os/AvCarb™ P75 in 10 mM $NaBH_4$–2 M NaOH (—), Os/AvCarb™ P75 in 2 M NaOH (- - -), (B) Os/GF-S3 in 10 mM $NaBH_4$–2 M NaOH (—), Os/ GF-S3 in 2 M NaOH (- - -). Scans started from −0.9 V_{SHE}, moving towards oxidizing potentials. Os loading for each electrode: 0.2 mg cm^{-2}, temperature: 298 K, scan rate: 10 mV s^{-1}. The 60th scans are presented.

51.7 eV and 54.4 eV likely indicate the presence of OsO_2, which is also supported by the literature [29–32,34]. The partial oxidation of the Os surface cannot be explained by anodic oxidation since the corresponding anodic peak expected at potentials greater than −0.3 V [24], was absent in the cyclic voltammograms (Fig. 5A and B). Thus, it is surmised the partial surface oxidation (OsO_2 formation) occurred during the electrode preparation procedure by exposure to ambient air.

3.4. DBFC experiments: comparison between the three-dimensional anodes at low Os loading (0.2 mg cm^{-2})

In Fig. 7, the fuel cell performance at 333 K of the two Os three-dimensional anodes with AvCarb™ P75 and GF-S3 substrates, respectively, are compared at an Os loading of 0.2 mg cm^{-2}. The AvCarb™ P75 electrode generated a superior peak power density compared to the GF-S3, namely 25.2 mW cm^{-2} versus 18.3 mW cm^{-2}. Both electrodes exhibited similar characteristics between cell voltages of 1.1 V (open circuit) and 0.9 V. The polarization curves differ at cell voltages below 0.9 V (Fig. 7). An explanation of this difference can be sought by calculating and comparing the effective ionic and electronic conductivities of the two three-dimensional electrodes and evaluating possible electrode kinetic differences.

The Bruggeman equation can be used to describe the effective ionic conductivity of a three-dimensional porous electrode:

$$\kappa = \kappa_0(\varepsilon)^{\frac{3}{2}} \quad (1)$$

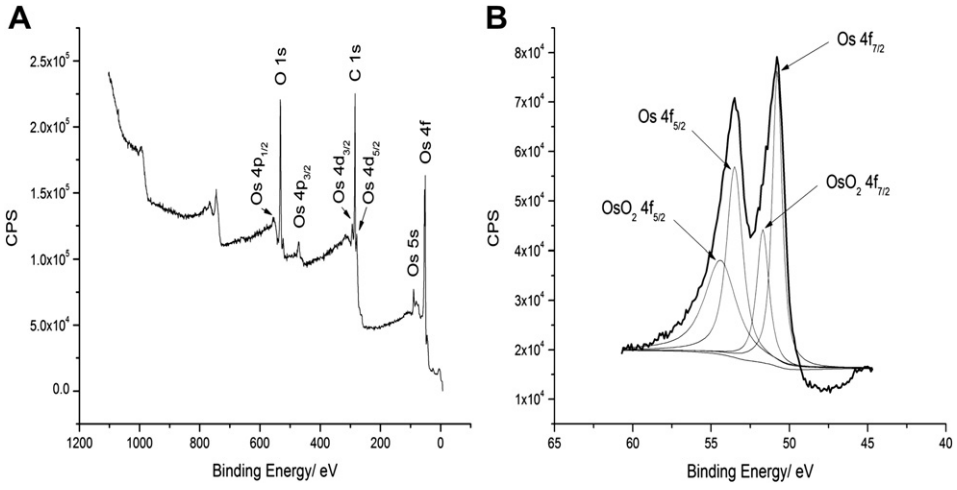

Fig. 6. (A) XPS wide scan of Os/AvCarb™ P75 and (B) XPS narrow scan of the same sample.

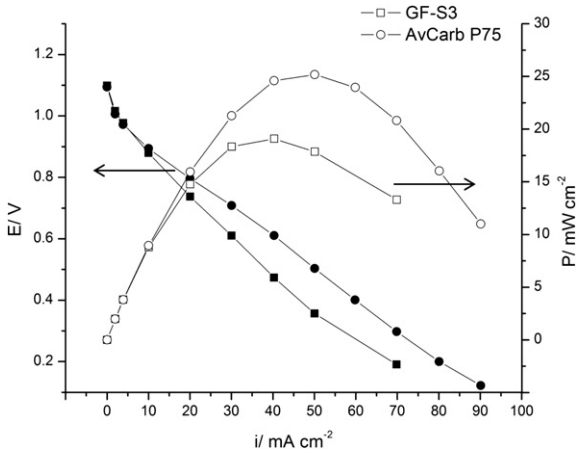

Fig. 7. Comparison of DBFC performance with Os/GF-S3 and Os/AvCarb P75 anodes. Os loading: 0.2 mg cm^{-2} for both anodes. Temperature: 333 K. cathode catalyst: 4 mg cm^{-2} Pt, O_2 pressure: 4.4 atm (abs), O_2 flow rate 0.25 SLPM, anolyte: 0.5 M $NaBH_4$–2 M NaOH, anolyte flow rate 10 mL min^{-1}.

where κ is the effective ionic conductivity of the three-dimensional electrode [S m^{-1}], κ_0 is the conductivity of the electrolyte (2 M NaOH) [S m^{-1}], and ε is the porosity of the substrate.

The AvCarb™ P75 is a denser material, with an average porosity of 0.85 and a thickness of 210 μm [35] whereas the GF-S3 has a porosity of 0.95 and a thickness of 350 μm [14]. It was assumed that both electrodes were compressed in the fuel cell to the same final thickness (approximately 100 μm), which was determined by the thickness of the gasket (Table 2). The ratio of the effective ionic conductivities was calculated with Eq. (2) and the results are shown in Table 2.

$$\kappa' = \frac{\kappa_{GF-S3}}{\kappa_{AvCarbP75}} = \left(\frac{\varepsilon_{GF-S3}}{\varepsilon_{AvCarbP75}}\right)^{3/2}. \quad (2)$$

The compressed porosity of the three-dimensional electrodes can be evaluated with a linear relationship:

$$\varepsilon = 1 - \frac{\tau_0(1-\varepsilon_0)}{\tau}, \quad (3)$$

where τ, τ_0 are the compressed and uncompressed thickness of the three-dimensional electrode, respectively, and ε_0 is the uncompressed (original) porosity of the substrates (AvCarb™ P75 and GF-S3, respectively).

From Table 2, it is clear that the GF-S3 three-dimensional electrode has a higher effective ionic conductivity than AvCarb™ P75. Therefore, the advantage of the Os/AvCarb™ P75 over the Os/GF-S3 anode at fuel cell voltages lower than 0.9 V (Fig. 7) cannot be explained by the effective ionic conductivity in the anode compartment.

The effective transverse electronic conductivity of a graphite fiber matrix such as GF-S3 and AvCarb™ P75 can be approximated by the following relationship [36]:

Table 2
Calculation of the effective ionic (κ') and electronic (σ') conductivity ratios of the GF-S3 to AvCarb™ P75 three-dimensional electrodes under the employed experimental conditions.

	Uncompressed electrode thickness (μm)	Compressed electrode thickness (μm)	κ'	σ'
GF-S3	350	100	1.25	0.45
AvCarb™ P75	210	100		

$$\sigma = 10 + 2800\left(1 - \frac{\varepsilon}{\varepsilon_0}\right)^{1.55} \quad 0.68 < \varepsilon/\varepsilon_0 < 1 \text{ at } 293\text{ K} \quad (4)$$

where σ is the effective electronic conductivity of the graphite fiber matrix, ε is the compressed porosity, and ε_0 is the uncompressed porosity.

It is likely that the parameters in Eq. (4) determined by fitting of experimentally measured electronic conductivity data [36], will differ based on the compositional and structural features of the employed carbon-based fiber matrix. In the absence of specific correlations for either AvCarb™P75 or GF-S3, Eq. (4) can provide a preliminary estimate of the respective electronic conductivities as a function of porosity. The ratio of the electronic conductivities is:

$$\sigma' = \frac{\sigma_{GF-S3}}{\sigma_{AvCarbP75}} \quad (5)$$

The calculations reveal that compressed AvCarb™P75 had about 2.2 times higher electronic conductivity compared to GF-S3, counteracting the approximately 25% lower effective ionic conductivity (Table 2). The higher effective electronic conductivity and possibly lower contact resistance with the end plate could have some benefits for the fuel cell polarization performance of Os/AvCarb™P75 in the ohmic potential loss controlled region.

An additional effect that probably is the most significant for cell voltages lower than 0.9 V in Fig. 7 is the accumulation and electrooxidation of surface adsorbed intermediate species such as BH_2OH_{ad} and/or BOH_{ad}. The fuel cell polarization data points are recorded in a sequential fashion hence, there is an in-built time factor in the polarization curves. The accumulation in time of strongly adsorbed species coupled with their sluggish oxidation will increase the anodic overpotential due to a higher effective (or apparent) Tafel slope, lowering the power output. As discussed in relation to the cyclic voltammetry study and peak "*c1*" (Fig. 5), Os/AvCarb™P75 was more effective in oxidizing the adsorbed intermediates. This beneficial electrode kinetic effect could have contributed to the superior fuel cell performance of the Os/AvCarb™P75 anode compared to Os/GF-S3 (Fig. 7).

3.5. DBFC experiments using Os/AvCarb™P75 anode: effect of temperature and Os loading

Based on Fig. 7, Os/AvCarb™P75 was retained as anode for further studies. A significant performance improvement was observed when the fuel cell temperature increased from 298 K to 333 K at an Os loading of 0.2 mg cm^{-2} (Fig. 8). Improvements in electrode kinetics, ionic conductivity and the open circuit voltage were all evident.

The positive effect of the increased temperature on the open circuit voltage is due to reduced mixed potential polarization losses on the cathode and/or anode. A mixed potential between BH_4^- and O_2 is established on the cathode due to BH_4^- crossover across Nafion® 117, whereas on the anode a mixed potential between BH_4^- and O_2 can form due to O_2 crossover. The O_2 cathode pressure was kept at 4.4 atm (abs) while the anode operated at approximately atmospheric pressure. The pressure differential minimized the BH_4^- crossover but it cannot be completely discounted. The mixed potential loss on the Pt cathode is lessened at higher temperature because of enhanced hydrolysis on Pt of the BH_4^- that crossed over to the cathode. As a result, the mixed potential polarization on the cathode will involve H_2–O_2 as opposed to the BH_4^-–O_2 couple. Furthermore, the structure of the three-dimensional electrode could also play a role in improving the open circuit voltage by reducing the BH_4^- crossover flux. The ability for three-dimensional electrodes to decrease fuel crossover has been proven by Lam et al.

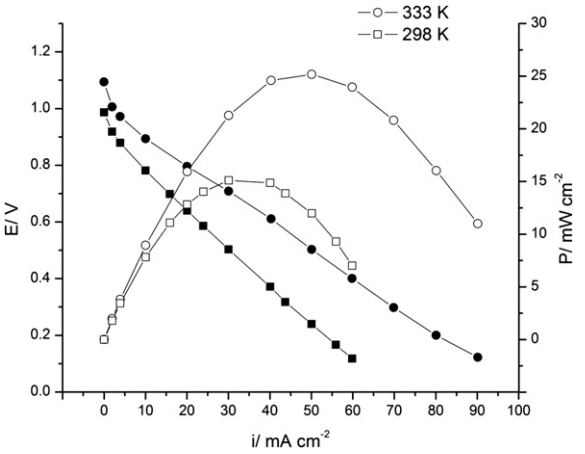

Fig. 8. Effect of temperature on DBFC operation with Os/AvCarb™ P75 anode with 0.2 mg cm^{-2} Os loading. Cathode catalyst: 4 mg cm^{-2} Pt, O_2 pressure: 4.4 atm (abs), O_2 flow rate 0.25 SLPM, anolyte: 0.5 M $NaBH_4$–2 M NaOH, anolyte flow rate 10 mL min^{-1}.

in a direct methanol fuel cell (DMFC) system [16]. They found that the open circuit voltage and methanol crossover of the DMFC improved with increased anode layer thicknesses.

In addition, another potential complicating factor on the anode could be the H_2 generated either by thermocatalytic hydrolysis of $NaBH_4$ (Eq. (6)) or incomplete electrooxidation of BH_4^-.

$$NaBH_4 + 2H_2O \rightarrow NaBO_2 + 4H_2 \quad (6)$$

If the rate of reaction (6) would be significant, it is expected that the presence of H_2 at the anode lowers the open circuit cell voltage by partially replacing the anodic reaction (7) with reaction (10), creating an in-situ alkaline hydrogen–oxygen fuel cell, (reaction (11)) instead of the direct fuel cell reaction (9). At higher temperatures the rate of the thermocatalytic hydrolysis (reaction (6)) is exponentially accelerated thereby enhancing the H_2 evolution. The fact that increasing the temperature from 298 K to 333 K increased the open circuit cell voltage as opposed to reducing it (Fig. 8), implies that the competing H_2 evolution/oxidation was probably not the predominant factor. At present, the relative rates as a function of temperature and concentration of borohydride hydrolysis (Eq. (6)) and direct BH_4^- and H_2 electrooxidations, respectively, are unknown on the electrodeposited Os catalysts and need to be separately investigated in future work. This would yield the effective borohydride utilization efficiency, which is an important figure of merit for the present system.

$$NaBH_4 + 8OH^- \rightarrow NaBO_2 + 6H_2O + 8e^- \; E^0_{a,I} = -1.24\,V_{SHE} \quad (7)$$

$$2O_2 + 4H_2O + 8e^- \rightarrow 8OH^- \; E^0_c = 0.4\,V_{SHE} \quad (8)$$

$$NaBH_4 + 2O_2 \rightarrow NaBO_2 + 2H_2O \; E^0_{cell,I} = 1.64\,V \quad (9)$$

$$4H_2 + 8OH^- \rightarrow 8H_2O + 8e^- \; E^0_{a,II} = -0.83\,V_{SHE} \quad (10)$$

$$4H_2 + 2O_2 \rightarrow 4H_2O \; E^0_{cell,II} = 1.23\,V \quad (11)$$

The effect of Os loading was tested in the case of Os/AvCarb™ P75 (Fig. 9). Higher Os loadings were achieved by simply repeating the electrodeposition process on the same substrate a number of times, using a fresh bath for each deposition step (see Section 2). Thus, Os loadings of 0.3, 0.9, and 1.7 mg cm^{-2} were achieved with single (1×), double (2×) and quadruple (4×) depositions, respectively. The corresponding peak power densities were 65.2 mW cm^{-2}, 75.9 mW cm^{-2}, and 102.8 mW cm^{-2}, respectively (Fig. 9). It is important to note that the specific peak power densities per Os loading, decreased with increasing Os loading: 203.8 mW g^{-1}, 89.3 mW g^{-1}, and 61.2 mW g^{-1} for 1×, 2×, and 4× depositions, respectively. The most probable explanation for this behavior is the increased agglomeration and reduced specific electrocatalytic surface area of Os as the loadings increased on the substrate.

Furthermore, Fig. 9 shows that the slope of the polarization curves gradually decreased with increase of the anode catalyst loading. This could be attributed to a decrease of the effective anodic Tafel slope at higher Os loadings, which is beneficial for the anode kinetic performance. Future studies should attempt the modeling of the three-dimensional Os anode DBFC polarization.

3.6. DBFC experiments using Os/AvCarb™P75 anode: experimental reproducibility and longer-term durability

The reproducibility of the anode performance was investigated by preparing three Os/AvCarb™ P75 electrodes by quadruple electrodeposition (loading of 1.7 mg cm^{-2}), and testing them under the same conditions in DBFC with the same cathode half-MEA each time (Fig. 10). The cathode half-MEA was washed with deionized water and purged with air between the repeated experiments.

The error bars in Fig. 10 represent the standard error of the mean at 90% confidence level [37]. At open circuit and current densities up to 100 mA cm^{-2} the error was small (virtually negligible), indicating that the electrodeposition procedure was generating reproducible Os catalytic surfaces with very similar electrode kinetic performance. The error in the measured cell voltage increased progressively with increasing current density, as ohmic and possibly mass transfer limitations gained more important roles (Fig. 10). Inherent structural differences among the AvCarb™ P75 samples used could have caused some morphological variations for the electrodeposited Os affecting the borohydride mass transport to the active sites. Furthermore, the reuse of the membrane and the cathode (i.e., half-MEA) could have generated somewhat deteriorating performance over time. The average peak power density was 109 mW cm^{-2} with a standard error of the mean ±12 mW cm^{-2} at 90% confidence level (Fig. 10). This error can be considered

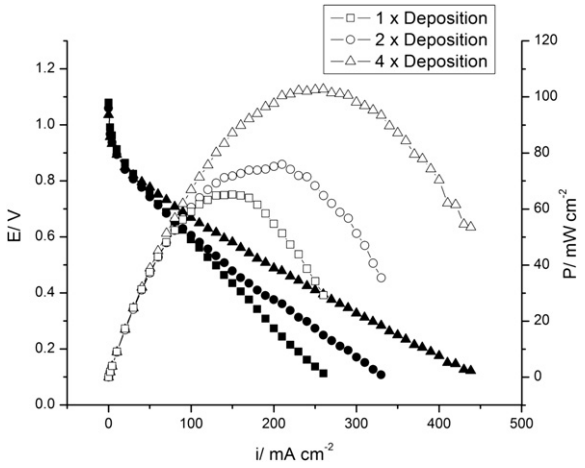

Fig. 9. Effect of Os loading on the DBFC performance with Os/AvCarb™ P75 anode. The Os loading was increased by repeating the electrodeposition process a number of times on the same substrate. Legend: (1×): single deposition, Os loading: 0.3 mg cm^{-2}, (2×): double deposition, Os loading: 0.9 mg cm^{-2}, (4×): quadruple deposition, Os loading: 1.7 mg cm^{-2}, Temperature: 333 K, cathode catalyst: 4 mg cm^{-2} Pt, O_2 pressure: 4.4 atm (abs), O_2 flow rate 1.25 SLPM, anolyte: 0.5 M $NaBH_4$–2 M NaOH, anolyte flow rate 10 ml min^{-1}.

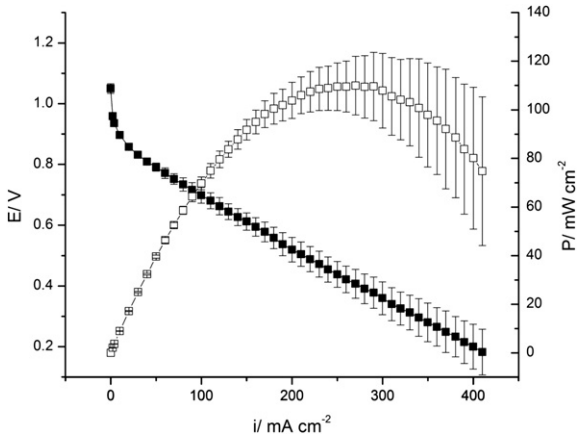

Fig. 10. Reproducibility of the DBFC performance with Os/AvCarb™ P75 anode prepared by the quadruple (4×) deposition procedure. Error bars represent the standard of the mean with 90% confidence level. Temperature: 333 K, cathode catalyst: 4 mg cm^{-2} Pt, O_2 pressure: 4.4 atm, O_2 flow rate 1.25 SLPM, anolyte: 0.5 M $NaBH_4$–2 M NaOH, anolyte flow rate 10 mL min^{-1}.

acceptable and shows good reproducibility for the electrodeposited Os three-dimensional anodes.

The longer-term performance of the DBFC equipped with Os/AvCarb™ P75 anode prepared by the quadruple electrodeposition procedure (see Figs. 9 and 10), was investigated at a constant current density of 290 mA cm^{-2} over a total operational time of 540 min, which was interrupted by two shutdowns of 12 h each, after 180 and 360 min, respectively (Fig. 11). After the first shutdown the fuel cell was not reconditioned in any form (such as by washing with distilled water or purging an inert gas at the cathode). During the first 180 minutes the DBFC cell voltage decreased by about 30 mV, which can be attributed to a slight deactivation of the Os catalytic surface over the first 180 min, amounting to approximately 10 mV h^{-1} voltage loss. This low Os degradation rate, due probably to the incomplete removal of some of the strongly adsorbed intermediates (as discussed before in relation to the cyclic voltammograms), was also confirmed in our previous study of DBFC with Os nanoparticle anode catalyst prepared by the modified Bönneman method and supported on Vulcan® XC72 [22].

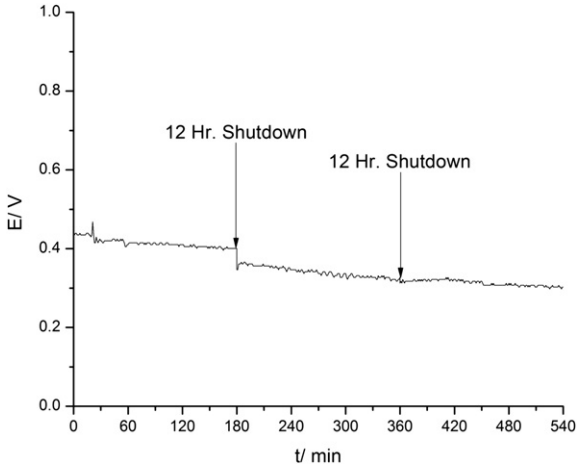

Fig. 11. Longer-term performance evaluation of the DBFC with Os/AvCarb™ P75 anode prepared by the quadruple (4×) deposition procedure. Os loading: 1.7 mg cm^{-2}. The DBFC was held at a constant current output of 290 mA cm^{-2}. Temperature: 333 K, cathode catalyst: 4 mg cm^{-2} Pt, O_2 pressure: 4.4 atm, O_2 flow rate 1.25 SLPM, anolyte: 0.5 M $NaBH_4$–2 M NaOH, anolyte flow rate 10 mL min^{-1}.

When the cell was restarted after 12 h shutdown, the voltage dropped by an additional 50 mV. It is hypothesized that the voltage loss at the first restart was due to crystallization and carbonation of the NaOH electrolyte particularly in the gas diffusion cathode which has narrower pores than the three-dimensional anode. This is a common occurrence in DBFC systems and in alkaline fuel cells and batteries in general [38,39]. To alleviate the cathode performance loss, after the second shutdown (i.e., after 360 min) the cathode compartment was washed with copious amounts of deionized water followed by drying with high flow rate of air. Therefore, following the second restart the cell voltage was the same as in the last portion of the previous operation sequence and it remained virtually constant for the last sequence of the testing period (between 360 and 540 min) (Fig. 11). Clearly, reconditioning the cathode was effective for recovering some of the performance.

4. Conclusion

Os three-dimensional electrodes were prepared by surfactant assisted electrodeposition on two graphite fiber substrates, AvCarb™ P75 and GF-S3, respectively. Due to the inherent morphological and compositional differences between the substrates, the Os deposit morphology and crystal structure were markedly different as well. On AvCarb™ P75, electrodeposition generated a polycrystalline Os with (100), (101), (103), (110) and (111) planes, whereas, on Os/GF-S3 only a relatively weak response from the (101) plane was detected by XRD. Further inspection via SEM and TEM revealed clusters of nano-sized deposits of Os with particle sizes equal to and less than 5 nm for both cases. XPS analysis showed that Os surface was partially oxidized.

Cyclic voltammetry of the Os three-dimensional electrodes in 10 mM $NaBH_4$–2 M NaOH solution revealed that both electrodes are active for BH_4^- oxidation, however, Os/AvCarb™ P75 was apparently kinetically superior especially with respect to oxidizing the strongly adsorbed intermediate species. The kinetic effect was correlated with the crystallography differences between the two electrodes.

The performance of the Os/AvCarb™ P75 and Os/GF-S3 anodes was compared in DBFC polarization experiments as well. At 333 K with 1.7 mg cm^{-2} Os loading obtained by four successive electrodeposition steps on AvCarb™ P75, the peak power density was 109 mW cm^{-2} with a standard error of ±12 mW cm^{-2} at 90% confidence level.

The present work also revealed areas for future studies such as the kinetic modeling of the BH_4^- electro-oxidation on Os three-dimensional electrodes coupled with experimental investigation of the thermocatalytic BH_4^- hydrolysis rate.

Acknowledgments

The authors thank the generous financial support of this work by the Natural Science and Engineering Research Council (NSERC) of the Government of Canada through the Discovery and Discovery Accelerator grant programs. The authors acknowledge Anita Lam for modeling of the XRD data, Maxxam Inc. for acquiring the ICP-MS data, and Surface Science Western for a portion of the XPS analysis and SEM images.

References

[1] J. Wee, J. Power Sources 161 (2006) 1.
[2] H. Cheng, K. Scott, J. Power Sources 160 (2006) 407.
[3] W.X. Yin, Z.P. Li, J.K. Zhu, H.Y. Qin, J. Power Sources 182 (2008) 520.
[4] J. Ma, N.A. Choudhury, Y. Sahai, Renew. Sustain. Energy Rev. 14 (2009) 183.
[5] Platinum Today, http://www.platinum.matthey.com [accessed December, 2011].

[6] V. Lam, A. Alfantazi, E. Gyenge, J. Appl. Electrochem. 39 (2009) 1763.
[7] T. Cheng, E. Gyenge, J. Appl. Electrochem. 38 (2008) 51.
[8] T.T. Cheng, E.L. Gyenge, J. Appl. Electrochem. 39 (2009) 1925.
[9] T.T. Cheng, E.L. Gyenge, J. Electrochem. Soc. 155 (2008) B819.
[10] A. Bauer, E.L. Gyenge, C.W. Oloman, J. Power Sources 167 (2007) 281.
[11] D.R. Lycke, E.L. Gyenge, Electrochim. Acta 52 (2007) 4287.
[12] A. Bauer, E.L. Gyenge, C.W. Oloman, Electrochim. Acta 51 (2006) 5356.
[13] T.T. Cheng, E.L. Gyenge, Electrochim. Acta 51 (2006) 3904.
[14] A. Bauer, C.W. Oloman, E.L. Gyenge, J. Power Sources 193 (2009) 754.
[15] A. Lam, B. Wetton, D.P. Wilkinson, J. Electrochem. Soc. 158 (2011) B29.
[16] A. Lam, D.P. Wilkinson, J. Zhang, Electrochim. Acta 53 (2008) 6890.
[17] A. Lam, M.S. Dara, D.P. Wilkinson, K. Fatih, Electrochem. Commun 17 (2012) 22.
[18] R.G. Allen, C. Lim, L.X. Yang, K. Scott, S. Roy, J. Power Sources 143 (2005) 142.
[19] R. Chetty, K. Scott, S. Kundu, M. Muhler, J. Fuel Cell Sci. Technol. 7 (2010) 031011.
[20] M.H. Atwan, D.O. Northwood, E.L. Gyenge, J. New Mater. Electrochem. Syst. 8 (2006) 243.
[21] M.H. Atwan, D.O. Northwood, E.L. Gyenge, Int. J. Hydrogen Energy 30 (2005) 1323.
[22] V.W.S. Lam, E.L. Gyenge, J. Electrochem. Soc. 155 (2008) B1155.
[23] M. Escano Clare Sison, E. Gyenge, R.L. Arevalo, H. Kasai, J. Phys. Chem. C 115 (2011) 19883.
[24] N. Takeno, Atlas of Eh-pH Diagrams – Intercomparison of Thermodynamic Databases, Report No. 419, National Institute of Advanced Industrial Science and Technology, May 2005.
[25] E. Gyenge, Electrochim. Acta 49 (2004) 965.
[26] V.W.S. Lam, D.C.W. Kannangara, A. Alfantazi, E.L. Gyenge, J. Phys. Chem. C 115 (2011) 2727.
[27] V.W.S. Lam, D. Kannangara, A. Alfantazi, E.L. Gyenge, Borohydride electro-oxidation on polycrystalline Pt electrodes. Regional Electrochemistry Meeting of South-East Asia, Bangkok, Thailand, November 17, 2010.
[28] D.A. Finkelstein, M. Da Nicolas, J.L. Cohen, H.D. Abruna, J. Phys. Chem. B 113 (2009) 19700.
[29] R. Liu, H. Iddir, Q. Fan, et al., J. Phys. Chem. B 104 (2000) 3518.
[30] Y. Zhu, C.R. Cabrera, Electrochem. Solid-State Lett. 4 (2001) A45.
[31] A. Hamnett, B.J. Kennedy, Electrochim. Acta 33 (1988) 1613.
[32] Y. Hayakawa, K. Fukuzaki, S. Kohiki, Y. Shibata, T. Matsuo, K. Wagatsuma, M. Oku, Thin Solid Films 347 (1999) 56.
[33] R. Zanoni, V. Carinci, R. Abu-Samn, R. Psaro, C. Dossi, J. Mol. Struct. 131 (1985) 363.
[34] D.D. Sarma, C.N.R. Rao, J. Electron. Spectrosc. Relat. Phenom. 20 (1980) 25.
[35] J.T. Gostick, M.W. Fowler, M.D. Pritzker, M.A. Ioannidis, L.M. Behra, J. Power Sources 162 (2006) 228.
[36] C. Oloman, M. Matte, C. Lum, J. Electrochem. Soc. 138 (1991) 2330.
[37] R.E. Walpole, R.H. Myers, S.L. Myers, Probability and Statistics for Engineers and Scientists, sixth ed. Prentice Hall, USA, 1972.
[38] R. Jamard, J. Salomon, A. Martinent-Beaumont, C. Coutanceau, J. Power Sources 193 (2009) 779.
[39] J.-F. Drillet, F. Holzer, T. Kallis, S. Müller, V.M. Schmidt, Phys. Chem. Chem. Phys. 3 (2001) 368.